

# Superradiant instability of massive vector fields around spinning black holes in the relativistic regime

William E. East

*Perimeter Institute for Theoretical Physics, Waterloo, Ontario N2L 2Y5, Canada*

We study the superradiant instability of massive vector fields, i.e. Proca fields, around spinning black holes in the test field limit. This is motivated by the possibility that observations of astrophysical black holes can probe the existence of ultralight bosons subject to this mechanism. By making use of time-domain simulations, we characterize the growth rate, frequency, spatial distribution, and other properties of the unstable modes, including in the regime where the black hole is rapidly spinning and the Compton wavelength of the Proca field is comparable to the black hole radius. We find that relativistic effects in this regime increase the range of Proca masses that are unstable, as well as the maximum instability rate. We also study the gravitational waves that can be sourced by such an instability, finding that they can be significantly stronger than in the massive scalar field case.

## I. INTRODUCTION

An intriguing possibility, that has been the focus of recent interest, is that spinning black holes could, in fact, be unstable because of the existence of ultralight massive bosons. This so-called superradiant instability relies on the wave analogue of the Penrose process, whereby waves with frequency  $\omega < m\Omega_H$ , where  $m$  is the azimuthal number of the wave and  $\Omega_H$  is the black hole horizon frequency, can superradiantly scatter off the black hole, gaining energy and angular momentum in the process. When this is combined with the fact that massive bosons can form gravitationally bound states around black holes, the “black hole bomb” originally proposed in [28] is realized: small (even vacuum) fluctuations of a massive boson can be exponentially amplified into large clouds that potentially gain some non-negligible fraction of the black hole’s rotational energy [12, 13, 35].

Hence, the superradiant instability allows astrophysical black holes to act as particle detectors of sorts, providing a unique method to look for weakly coupled, ultralight massive bosons such as the string axiverse [6, 7], the QCD axion [4, 5], or dark/massive photons [22, 27]. The superradiant instability is strongest for particles with a Compton wavelength that is comparable to the radius of a given black hole, where particles masses in the range  $\sim 10^{-10}$  to  $10^{-18}$  eV are probed by black holes with masses  $\sim 1$  to  $10^8 M_\odot$ . In light of the recent observations of gravitational waves (GWs) from merging black holes by LIGO [1, 2], with many more expected in the coming years as LIGO reaches design sensitivity [3], measuring black hole masses and spins from GW observations is one promising avenue for ruling out, or providing evidence for, the existence of such ultralight massive fields [4, 8]; in addition the oscillating bosonic clouds

that form from the superradiant instability can be a source of nearly monochromatic GWs, which could also be detectable.

There have been numerous studies of the superradiant instability of massive scalar fields around spinning black holes [4, 5, 7, 10, 14], including time-domain simulations [15, 32], and studies of the gravitational radiation produced [33]. Though massive vector fields, i.e. Proca fields, can have significantly faster rates of superradiant growth around a spinning black hole than scalar fields, their treatment is more difficult since, even at the level of a test field, the equations do not decouple in the Teukolsky formalism. There have been studies specializing to a nonspinning black hole [20, 24, 25, 30], making use of a slow rotation approximation for the black hole [26, 27], using effective field theory methods [19], and recent work using a matching procedure [8] to analytically calculate the instability rate in the nonrelativistic limit. However, a complete picture of the superradiant instability for massive vectors in the relativistic regime, where the Compton wavelength of the field is comparable to the black hole radius—which is also the regime where the instability rate will be largest—has been lacking.

Here we attempt to address this by making use of time-domain simulations of the full Proca equations on Kerr spacetimes. In [32], a full 3 + 1 simulation of such a case was performed, illustrating the superradiant instability in the relativistic regime. (See also [34] for a study of the nonlinear behavior of Proca fields around nonspinning black holes.) However, the computational expense of such simulations makes it difficult to follow such evolutions for very long times, or to explore the parameter space. Here we use a similar approach, but by fixing the azimuthal symmetry of the field, we are able to reduce the computational domain to two dimensions, which allows us to evolve

the fields for time scales of  $\sim 10^5$  times the horizon crossing time of the black hole, and thus to clearly determine the properties of the superradiant instability across a range of parameters. We find that the Proca field superradiant instability growth rate can be quite fast, with, for example, the Proca field energy having a minimum  $e$ -folding time of  $\sim 70(M/10M_\odot)$  ms for a black hole spin of mass  $M$  and dimensionless spin  $a = 0.99$  (for a Proca field with azimuthal number  $m = 1$ ), and about 20 longer for the next lowest azimuthal number ( $m = 2$ ). We show that relativistic effects extend the range of mass parameters over which the Proca field is unstable by decreasing the frequency of the bound states relative to the nonrelativistic approximation, and come up with a simple approximation for these corrections. We also study the properties of the superradiantly unstable Proca field modes, including the gravitational radiation that they can source, finding that the GW luminosity in the relativistic regime can be much higher than in the equivalent scalar field case.

The rest of the paper is organized as follows. In Sec. II we summarize the Proca field equations and the numerical methods we use for evolving them, and define the quantities used for analyzing the superradiant instability; in Sec. III we present results for the superradiant instability including the growth rate, frequency, mass range frequency, spatial distribution, and GW signal of the unstable modes; in Sec. IV we discuss these results, compare them to others in the literature, and conclude with some directions for future work; in the Appendix we provide some details on numerical convergence and error estimates.

## II. METHODS

In this paper, we study the evolution of Proca fields on a fixed Kerr spacetime with mass  $M$  and dimensionless spin  $a$ . We use Cartesian Kerr-Schild coordinates [23] where the spacetime metric is given by

$$ds^2 = -dt^2 + dx^2 + dy^2 + dz^2 + \frac{2Mr^3}{r^4 + a^2M^2z^2} \left[ dt + \frac{z}{r} dz + \frac{r}{r^2 + a^2M^2} (xdx + ydy) - \frac{aM}{r^2 + a^2M^2} (xdy - ydx) \right]^2,$$

where  $(x^2 + y^2)/(r^2 + a^2) + z^2/r^2 = 1$ . Here and throughout we use units with  $G = c = 1$ .

We consider a complex Proca field  $X_a = X_a^R + iX_a^I$  (or equivalently, two uncoupled real Proca fields) with

equation of motion

$$\nabla_a F^{ab} = \mu^2 X^b, \quad (1)$$

where  $F_{ab} = \nabla_a X_b - \nabla_b X_a$  and  $\mu$  is the Proca field mass.

Following [11], in order to make the problem numerically tractable, we will assume that the Proca field has a specific azimuthal dependence which will allow us to make our computational domain two dimensional. Let  $\mathcal{L}_\phi$  be the Lie derivative with respect to the usual axisymmetric Killing vector of the Kerr spacetime. Then we will assume that

$$\mathcal{L}_\phi X_a = imX_a, \quad (2)$$

where  $m$  is a non-negative integer (below we will study  $m = 1$  and 2). We then use a generalization of the modified cartoon method introduced in [29] where we take our numerical domain to be the two-dimensional half plane given by  $0 \leq x < \infty$  and  $-\infty < z < \infty$ . Derivatives in the  $y$  direction are calculated by rewriting them in terms of  $x$  and  $z$  derivatives using Eq. 2, and regularity is imposed at the  $z$  axis. In Sec. III D we also perform a few shorter simulations of the Einstein-Proca equations with just a real-valued Proca field in a fully three-dimensional computational domain to study GW production.

As in [34], we use a 3+1 decomposition of  $X_a$  into a scalar  $\chi$  and a three vector  $\chi_i$ ,

$$X_a = \chi_a + n_a \chi, \quad (3)$$

where  $n_a$  is the unit vector perpendicular to slices of constant coordinate time, and introduce an electric field

$$E_i = \gamma_i^a F_{ab} n^b, \quad (4)$$

where  $\gamma_b^a = \delta_b^a + n^a n_b$  is the spatial projection operator. Also as in [34], we introduce an auxiliary scalar field  $Z$  to dampen violations of the Proca field-equivalent of the Gauss constraint at some prescribed rate  $\sigma$ . We then evolve the real and imaginary parts of the variables  $\{\chi, \chi_i, E^i, Z\}$  according to

$$\alpha^{-1}(\partial_t - \mathcal{L}_\beta)\chi_i = -E_i - \partial_i \chi - \chi \partial_i \log \alpha, \quad (5)$$

$$\alpha^{-1}(\partial_t - \mathcal{L}_\beta)\chi = K\chi - D_i \chi^i - \chi^i \partial_i \log \alpha - Z, \quad (6)$$

$$\alpha^{-1}(\partial_t - \mathcal{L}_\beta)E^i = KE^i + D^i Z + \mu^2 \chi^i + \epsilon^{ijk} D_j B_k - \epsilon^{ijk} B_j \partial_k \log \alpha, \quad (7)$$

$$\alpha^{-1}(\partial_t - \mathcal{L}_\beta)Z = D_i E^i + \mu^2 \chi - \sigma Z, \quad (8)$$

where  $\alpha$  and  $\beta^i$  are the lapse and shift, respectively,  $K$  is the trace of the extrinsic curvature,  $D_i$  is the

covariant derivative associated with the spatial metric,  $\epsilon_{ijk}$  is the spatial totally antisymmetric tensor, and  $B^i = \epsilon^{ijk} D_j \chi_k$  is the magnetic field. We evolve these equations on the Kerr spacetime using fourth-order Runge-Kutta time stepping and standard fourth-order stencils for spatial derivatives.

For our numerical grid, we use seven levels of mesh refinement, with 2:1 refinement ratio, centered on the black hole. For the results presented below, we use a grid with  $96 \times 192$  points on each mesh refinement level and a corresponding resolution of  $dx/M \approx 0.0256$  on the finest level, or better. More details on the resolution, as well as numerical convergence and error estimates are given in the Appendix.

### A. Measured quantities

The energy-momentum tensor associated with the Proca fields is given by

$$T_{ab} = \frac{1}{2}(F_{ac}\bar{F}_{bd} + \bar{F}_{ac}F_{bd})g^{cd} - \frac{1}{4}g_{ab}F_{cd}\bar{F}^{cd} + \frac{\mu^2}{2}(X_a\bar{X}_b + \bar{X}_aX_b - g_{ab}X_c\bar{X}^c), \quad (9)$$

where the overbar indicates complex conjugation. Using the time and axisymmetric Killing vectors of the Kerr spacetime, we can define an energy

$$E := \int -T_t^t \sqrt{-g} d^3x := \int \rho_E \sqrt{\gamma} d^3x \quad (10)$$

and angular momentum

$$J := \int T_\phi^t \sqrt{-g} d^3x := \int \rho_J \sqrt{\gamma} d^3x \quad (11)$$

for the Proca field (where  $g$  and  $\gamma$  are the determinants of the four- and three-metric, respectively), along with associated energy and angular momentum densities on slices of constant coordinate time. We will make use of these quantities, evaluated in the exterior of the black hole horizon. Any change in  $E$  and  $J$  will be due to a flux of these quantities through the black hole horizon, which can be calculated in terms of surface integrals over the horizon:

$$\dot{E}^H = \int -\alpha T_t^i dA_i \quad (12)$$

and

$$\dot{J}^H = \int \alpha T_\phi^i dA_i. \quad (13)$$

## III. RESULTS

### A. Onset of linear instability

In order to study the superradiant instability we start with some, essentially arbitrary, initial data and evolve it until the solution becomes dominated by the most unstable mode (consistent with the specified azimuthal symmetry). We illustrate this in Fig. 1 where we show the energy and angular momentum of the Proca field as a function of time for several cases with  $a = 0.99$ ,  $m = 1$ , and  $\tilde{\mu} := M\mu = 0.3, 0.4$ , and  $0.5$ . After a transient phase, the solution clearly settles into exponential growth allowing for the instability growth rate and other properties of the dominant unstable mode to be measured. For these cases we find that the energy and angular momentum grow as  $e^{2\omega_I t}$  (where the factor of 2 is included since the energy and angular momentum are quadratic in the fields) with  $M\omega_I \approx 7 \times 10^{-5}$ ,  $2 \times 10^{-4}$ , and  $3 \times 10^{-4}$  for  $\tilde{\mu} = 0.3, 0.4$ , and  $0.5$ , respectively. Here we use initial data given by  $\chi_x = -i\chi_y = Ae^{-r/r_0}/\gamma^{1/2}$  and  $\chi_z = \chi = E^i = 0$ , though other configurations give similar results (but may take longer for the most unstable mode to clearly emerge). As shown in Fig. 2, as the most unstable mode dominates, the ratio of Proca field energy to angular momentum becomes roughly constant. Correspondingly, the ratio of the flux in energy and angular momentum across the black horizon settles to another (albeit somewhat noisier) measure of this same value. This can be used as a measure of the real part of the frequency  $\omega_R$  of the unstable mode.

In the remainder of this paper, we will concentrate on properties of the dominant unstable mode for various values of the Proca field mass,  $0.18 \leq \tilde{\mu} \leq 1.1$ ; black hole spin,  $0.7 \leq a \leq 0.99$ ; and azimuthal number,  $m = 1$  and  $2$ . For comparison, we recall the results in the literature obtained in the limit of  $\tilde{\mu} \ll 1$ , where the bound modes of the Proca field resemble that of a hydrogen atom [8, 19, 20, 27, 30]. Since here we look for the fastest growing mode with a given value of  $m$  (1 or 2) we expect to see the  $m = j = \ell + 1$  modes where  $j$  and  $\ell$  are, respectively, the total and angular momentum quantum numbers (using the notation of [8]). These particular bound states have real frequency given by  $\omega_R \approx \mu[1 - (\tilde{\mu}/m)^2/2]$  and a growth rate that is proportional to  $\tilde{\mu}^{4m+3}M^{-1}$  for sufficiently small  $\tilde{\mu}$ . The mode functions fall off exponentially with characteristic length scale  $(M\mu^2)^{-1}$ , and the dominant  $m = 1$  mode has spatial vector  $X_i \propto e^{-rM\mu^2}(\hat{x} + i\hat{y})e^{-i\omega t}$ .

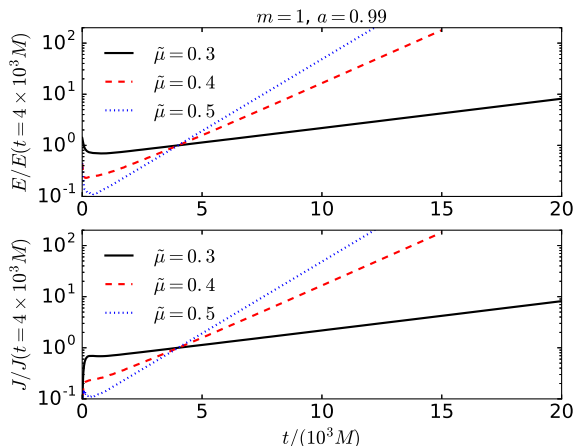


FIG. 1. The energy (top) and angular momentum (bottom) in the Proca field as a function of time for cases with  $m = 1$  and a black hole with spin  $a = 0.99$ . After a short transient period, the evolution is dominated by an exponentially growing mode.

### B. Frequency and growth rate

To begin, we focus on cases with azimuthal dependence  $m = 1$  and nearly extremal black hole spin  $a = 0.99$ —both of which maximize the growth rate of the superradiant instability—and consider a range of Proca field masses. The results for the frequency  $\omega_R := E/J$  and growth rate are shown in Fig. 3. For smaller values of  $\tilde{\mu}$  we find that  $\omega_R/\mu \approx 1 - \tilde{\mu}^2/2$  as expected in the nonrelativistic limit where the spectrum of the bound states resembles that of a hydrogen atom in quantum mechanics [14]. Furthermore, we find a faster decrease in  $\omega_R/\mu$  for larger  $\mu$  which is well approximated by the addition of a  $\mu^3$  term, i.e. by

$$\omega_{\text{Fit}} = \mu \left[ 1 - (\tilde{\mu}/m)^2/2 - 0.33(\tilde{\mu}/m)^3 \right], \quad (14)$$

where the last coefficient was found by fitting to the measured points. Here  $m = 1$ , but we keep  $m$  in the expression for use below, as we find that this fitting form also approximates the  $m = 2$  data, as well as lower spins.

As shown in the bottom panel of Fig. 3, we find that Proca fields with  $\tilde{\mu} \lesssim 0.54$  are unstable, while for large values of  $\tilde{\mu}$  the field decays. The maximum instability growth rate for  $a = 0.99$  is  $M\omega_I \approx 3.6 \times 10^{-4}$  (with the growth rate for the energy being twice that) and is achieved for  $\tilde{\mu} \approx 0.47$ . For sufficiently small  $\tilde{\mu}$ , we expect  $M\omega_I \propto \tilde{\mu}^7$  while at larger  $\mu$  the instability rate should switch signs (and become a decay rate) when

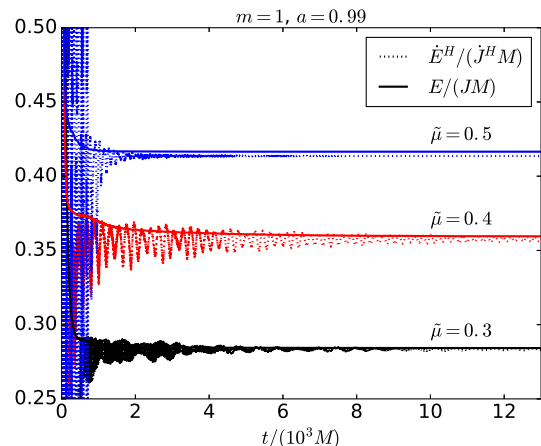


FIG. 2. The ratio of the energy to angular momentum in the Proca field  $E/J$ , and the ratio of the energy flux to angular momentum flux  $\dot{E}^H/J^H$  through the black horizon, as a function of time for cases with  $\tilde{\mu} = 0.3, 0.4$ , and  $0.5$ ,  $m = 1$ , and a black hole with spin  $a = 0.99$ . After the onset of the instability, this ratio settles to a roughly constant value which can be used as a measure of the frequency  $\omega_R$  of the dominant unstable mode.

$\omega_R = m\Omega_H$ . Combining this with the above function  $\omega_{\text{Fit}}(\mu)$ , and fitting for the overall factor (which we find to be close to unity)  $A \approx 1.0$  using the unstable points, we obtain a decent approximation for the growth or decay rate of the dominant Proca mode in this regime with

$$[M\omega_I]_{\text{Fit}} = A(\tilde{\mu}/m)^{4m+3} [a - 2r_+\omega_{\text{Fit}}/m], \quad (15)$$

where here  $m = 1$ . This is the dotted line in the bottom panel of Fig. 3.

#### 1. Spin dependence

We also consider the behavior of the instability growth rate as a function of black hole spin. Fixing  $m = 1$  and considering several values of  $\tilde{\mu}$ , we obtain the results shown in Fig. 4. For a fixed value of  $\tilde{\mu}$ , the instability rate decreases with decreasing spin, and when  $\Omega_H < \omega_R/m$ , superradiance shuts off. However when  $\omega_R$  is not near  $m\Omega_H$ , the dependence of the instability rate on spin is not that strong; for example, for  $\tilde{\mu} = 0.2$ , the instability rate only decreases by  $\sim 50\%$  going from  $a = 0.99$  to  $a = 0.8$ .

For comparison in Fig. 4 we also show an extrapolation of the spin dependence of the instability of the form  $\omega_I \propto r_+(1 - \omega_{\text{Fit}}/\Omega_H)$ . The choice of this func-

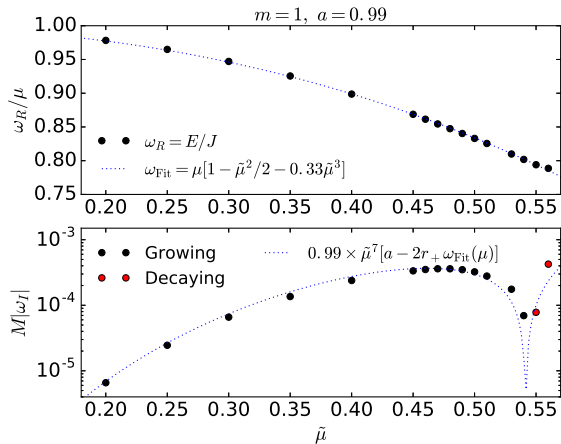


FIG. 3. Measured values of the frequency of the dominant unstable mode for  $m = 1$ ,  $a = 0.99$ , and various values of  $\tilde{\mu}$ . Top panel: The real part of the frequency as measured from the ratio of the energy to angular momentum along with the fitting function given by Eq. (14). Bottom panel: The growth (black points) or decay (red points) rate of the dominant mode of the Proca field along with the fitting function given by Eq. (15).

tional form from among other functions that decrease with decreasing  $a$  (for the values of  $\mu$  shown) and go to zero when  $\omega_R \rightarrow \Omega_H$  was made more or less arbitrarily, and it seems to overestimate the spin dependence at large spins for the higher Proca field masses, but provides a decent match for  $\tilde{\mu} = 0.2$ . In Fig. 5 we show the real and imaginary frequency of the dominant Proca field modes for  $a = 0.7$ . The dependence of frequency on  $\mu$  is also approximately captured by Eq. (14) obtained above from the  $a = 0.99$  results, which is also shown in Fig. 5. For the instability rate, we also fit the functional form given by Eq. (15) to these few unstable points and find a higher coefficient than in the  $a = 0.99$  case,  $A \approx 2.3$ .

## 2. Modes with $m = 2$

Next we consider Proca field modes with one higher azimuthal number:  $m = 2$ . The maximum instability rate for these modes is significantly smaller than for  $m = 1$ , though they are unstable for larger values of  $\tilde{\mu}$ . We show results for  $a = 0.99$  and various values of  $\tilde{\mu}$  in Fig. 6. Here we find that Proca fields with  $\tilde{\mu} \lesssim 1.05$  are unstable. The maximum growth rate for  $m = 2$  and  $a = 0.99$  is  $M\omega_I \approx 2 \times 10^{-5}$  and is achieved for  $\tilde{\mu} \approx 0.98$ . This is roughly a factor of 20 slower than the  $m = 1$  case. Again we find that  $\omega_R$

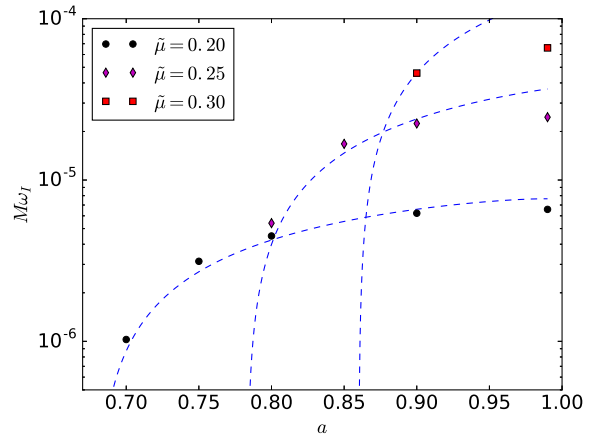


FIG. 4. The  $m = 1$  instability growth rate as a function of black hole spin for several values of the Proca mass. The dotted blue line shows the dependence  $\omega_I \propto r_+(1 - \omega_R/\Omega_H)$  with the amplitude fit to the  $a \leq 0.9$  points.

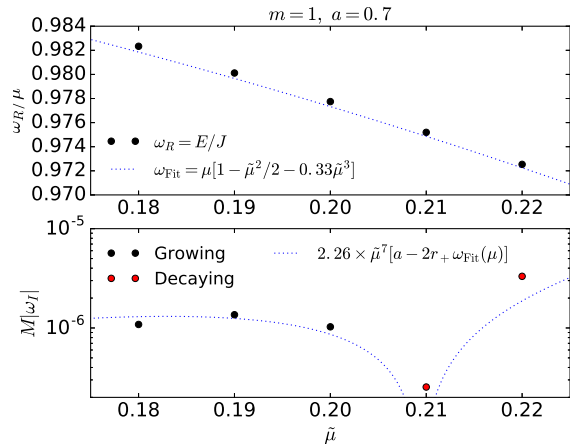


FIG. 5. The same as Fig. 3, but for a black hole with spin  $a = 0.7$ . The dotted blue line in the top panel ( $\omega_{\text{Fit}}$ ) is the fit from the  $a = 0.99$  data in Fig. 3 (not the data shown in this figure).

is well approximated by the expression in Eq. (14), but now with  $m = 2$ . In Fig. 6 we also show the approximation given by Eq. (15) for the instability rate, this time with  $m = 2$ , which approximates the trend with a best-fit amplitude of  $A \approx 1.1$ .

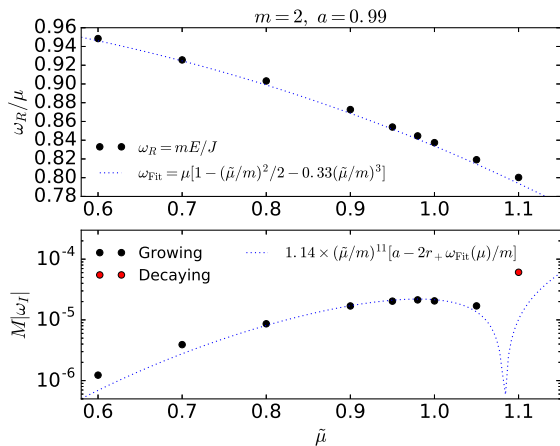


FIG. 6. Similar to Fig. 3, but for modes with  $m = 2$  (and  $a = 0.99$ ). Top panel: The real part of the frequency as measured from  $\omega_R = 2E/J$ , along with Eq. (14) (which was obtained by fitting to the data in Fig. 3). Bottom panel: The growth (black points) or decay (red points) rate of the dominant mode of the Proca field along with the fitting function.

### C. Unstable mode

In addition to the frequency and instability rate, we can also characterize the spatial structure of the dominant unstable modes. In general, for smaller values of  $\tilde{\mu}$ , the modes will have larger characteristic length scales, and be less concentrated near the black hole horizon. This is illustrated in Fig. 7 where we show the energy density  $\rho_E$  on the equatorial plane for various values of  $\tilde{\mu}$ . We can see that the Proca field in the clouds falls off exponentially at large distances, and with characteristic length  $1/(M\mu^2)$  (or twice this value for the energy) for smaller values of  $\tilde{\mu}$ , as expected for bound states in the hydrogen atom approximation. Here and below, the overall normalization of the unstable mode is arbitrary.

We also show the energy and angular momentum density for three representative cases with  $\tilde{\mu} = 0.2, 0.5, \text{ and } 0.95$ , and  $m = 1, 1, \text{ and } 2$ , respectively, in Fig. 8. Farther away from the black hole, and in particular for the lower  $\mu$  cases, the Proca cloud energy density is roughly spherical. However, near the black hole the Proca cloud shows deviations from sphericity. This is illustrated in Fig. 9, where it can be seen that as  $\mu$  increases the unstable mode becomes concentrated in a smaller and smaller region around the black hole equator.

We also show streamline plots for the spatial pro-

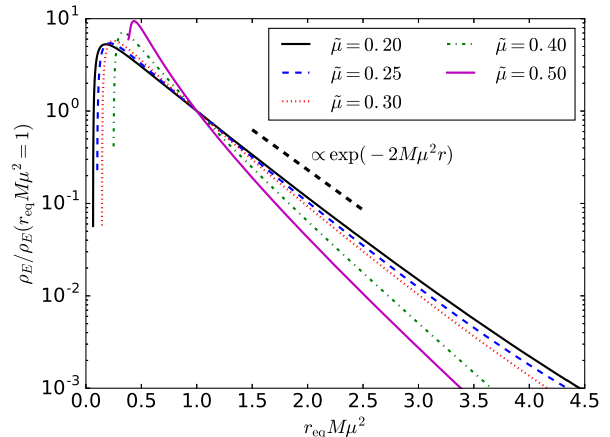


FIG. 7. The falloff of energy density along the equator for cases with  $m = 1$ ,  $a = 0.99$  and various values of  $\mu$ . The equatorial radius is multiplied by  $M\mu^2$  which sets the length scale, and for smaller values of  $\mu$  the falloff of energy goes like  $\exp(-2M\mu^2 r_{\text{eq}})$ .

jection of the potential vectors of the dominant unstable modes for representative cases in Fig. 10. Over large distances, the vector field points in a roughly constant direction (at a given instance of time), as expected from the hydrogenic approximation. In the vicinity of the black hole, the field lines curve more strongly, though this may in part be an artifact of the particular coordinates used here.

### D. Gravitational waves

In this section we address what the GW signal would be from a superradiantly unstable Proca field. Above we have considered configurations of a complex Proca field with an azimuthal symmetry which leads to an axisymmetric stress energy tensor. At the test field level, this is mainly for computational convenience since the real and imaginary parts of the Proca field are uncoupled. However, when coupled to gravity such a source will produce very little gravitational radiation. But if we instead consider just a single real Proca field, the oscillation of the unstable mode around the black hole will produce GWs at a frequency  $2\omega_R$ . In order to calculate the magnitude of this, we take the Proca field configuration from a simulation that has evolved sufficiently long for the most unstable mode to dominate, and then use just the real part of the Proca field as initial data for a fully three-dimensional simulation where we evolve

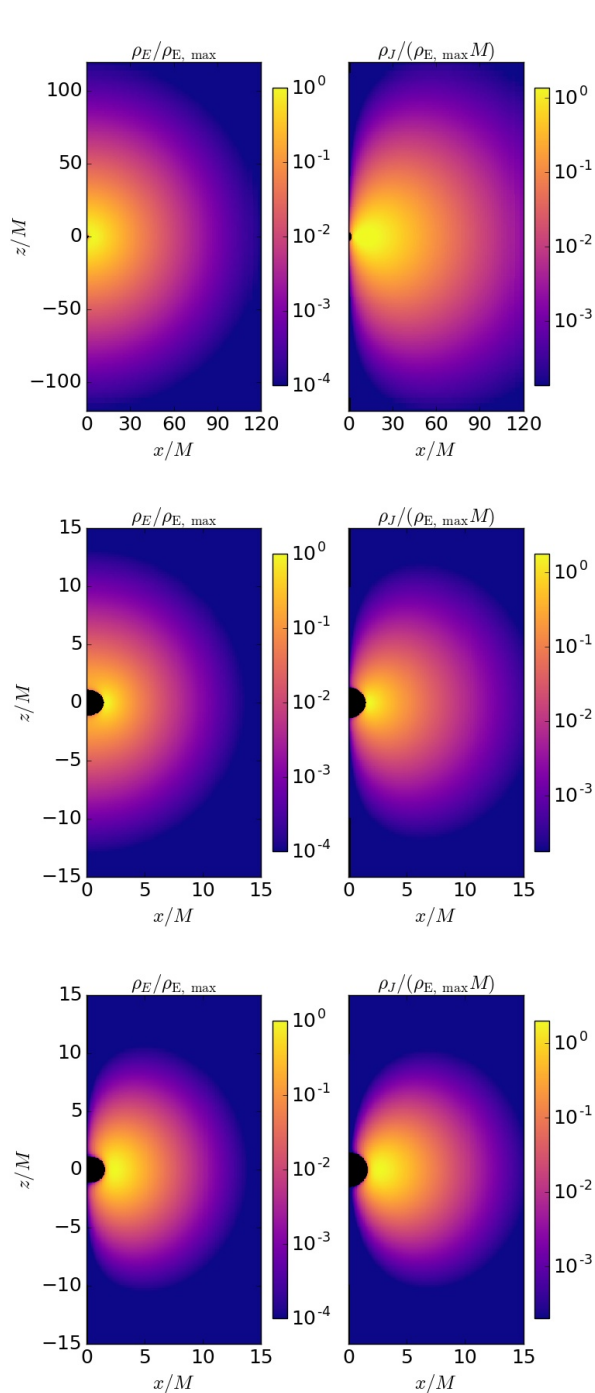


FIG. 8. Energy (left) and angular momentum density (right) for cases with a black hole with  $a = 0.99$  and (from top to bottom)  $\tilde{\mu} = 0.2, 0.5,$  and  $0.95$ , and  $m = 1, 1,$  and  $2$ , respectively. The  $z$  axis is the spin axis of the black hole and  $z = 0$  is the equatorial plane. Note the difference in spatial scales between the top and bottom two cases.

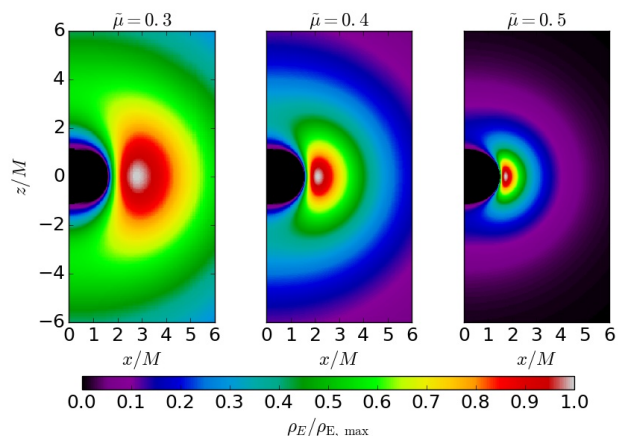


FIG. 9. Energy density near the black hole for cases with  $m = 1$ ,  $a = 0.99$ , and  $\tilde{\mu} = 0.3, 0.4,$  and  $0.5$  (left to right). The  $z$  axis is the black hole spin axis.

both the Proca field and the Einstein field equations. For all cases we scale the amplitude of the Proca fields so that the initial energy is  $E/M \leq 10^{-3}$ , and ignore the self-gravity of the Proca field in the initial data for the metric. We evolve the Einstein equations using the background error subtraction technique as described in [16] to minimize the truncation error from just the spinning black hole solution. After a brief transient period, this produces a nearly monochromatic GW signal which we measure by extracting the Newman-Penrose scalar  $\Psi_4$ .

In Fig. 11 we show the GW luminosity for  $m = 1$ ,  $a = 0.99$ , and several values of  $\tilde{\mu}$ <sup>1</sup>. The GW luminosity has been scaled with the square of the energy in the Proca field, so as to be independent of the Proca field magnitude in the test field limit (which we have verified to be approximately true for the values used here). The gravitational radiation is primarily quadrupolar, i.e. when performing a decomposition into spin-2 spherical harmonics, the  $\ell = |m| = 2$  components dominate. In Fig. 11 we also show the contribution from higher  $\ell$  components of the GW signal (still with  $|m|=2$ ), which make a larger contribution for larger  $\mu$  cases where the Proca cloud is localized

<sup>1</sup>The resolution we use for these three-dimensional simulations to determine the GWs is equivalent to the “medium” resolution of [18]. From one simulation at lower resolution for the  $\tilde{\mu} = 0.4$ , we estimate the truncation error in  $P_{\text{GW}}$  to be  $< 10\%$  and to primarily be an underestimate of the power due to the numerical dissipation of the GWs in the wave zone, which will be less severe for the lower  $\tilde{\mu}$  cases, which have longer wavelength GWs.

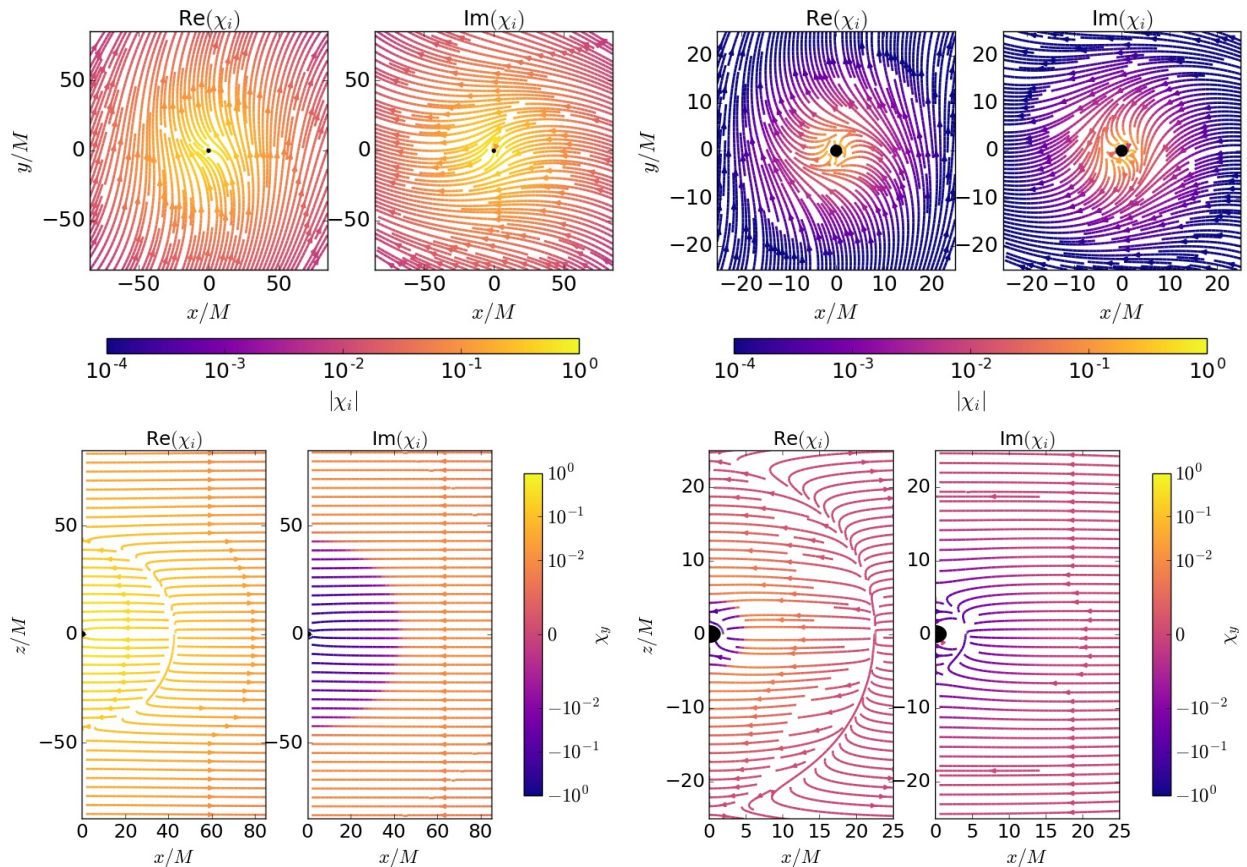


FIG. 10. Streamlines of the real and imaginary parts of  $\chi_i$  in the equatorial plane ( $z = 0$ ; top), and in the  $y = 0$  plane (bottom) for snapshots from  $m = 1$ ,  $a = 0.99$ , and  $\tilde{\mu} = 0.2$  (left) and  $0.5$  (right). Note the difference in scales in the two cases.

closer to the black hole and less spherical. For the highest mass parameter considered,  $\tilde{\mu} = 0.5$ , the  $\ell = 3$  contribution is comparable to the  $\ell = 2$ . This is similar to what was found for the dominant superradiantly unstable mode in the massive scalar field case, though the overall magnitude of the GW power found here for vector fields  $P_{\text{GW}} \sim 10^{-4}(E/M)^2$  is significantly larger than the  $\sim 10^{-8}$  values found in the scalar case for  $a = 0.99$  and the regime of the maximum instability [33]. For the smaller values of  $\tilde{\mu}$  where the Proca cloud is concentrated on scales large compared to the black hole radius, these results should not be very sensitive to the black hole spin, and we have verified that for  $\tilde{\mu} = 0.2$ , the values of  $P_{\text{GW}}$  for  $a = 0.7$  and  $a = 0.99$  differ by  $< 10\%$ .

Since the GW luminosity is proportional to the square of the Proca cloud energy, while the superradiant growth rate is directly proportional to the energy, the importance of GW emission will increase as

the cloud grows. However, as can be seen by comparison with the instability growth rate (also shown in Fig. 11 at a reference energy of  $E = M$ ), it does not appear that GW emission will significantly reduce the growth rate of the Proca cloud due to superradiance, even up to the maximum saturation energies of  $E \approx 0.09M$  [17], for these parameters. Though we do not consider very small values of  $\tilde{\mu}$ , the GW luminosity (divided by the Proca energy squared) appears to be falling off more steeply with decreasing  $\mu$  than the instability rate—slightly steeper than  $\tilde{\mu}^8$  from the few points measured, versus  $\tilde{\mu}^7$  for the instability rate—indicating that GW emission will be less significant at lower values of the mass parameter. The calculation of the GW power in the small  $\tilde{\mu}$  limit performed in [8] indicates that  $P_{\text{GW}} \times (M/E)^2$  should fall off even more steeply,  $\propto \tilde{\mu}^{10}$  in that regime. The value for the GW luminosity we find here for  $\tilde{\mu} = 0.2$  falls between the estimates obtained in the “flat-space” approxima-



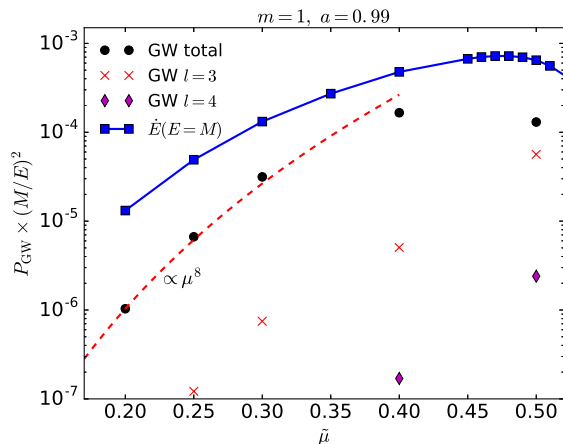


FIG. 11. The GW power as a function of  $\tilde{\mu}$  for the dominant  $m = 1$  unstable mode consisting of a single real-valued Proca field around an  $a = 0.99$  black hole (black points). In addition to the total GW power, which predominately comes from the  $(\ell, m) = (2, \pm 2)$  components, we also show the contributions from the  $(\ell, m) = (3, \pm 2)$  (red Xs) and  $(\ell, m) = (4, \pm 2)$  (magenta diamonds) spin-2 spherical harmonics. The GW power has been divided by the square of the Proca field energy so as to be independent of the magnitude of the mode, in the test field limit. For comparison we also show the superradiant instability growth rate of energy, at a reference energy of  $E = M$  (blue squares). The ratio of GW luminosity to the superradiant growth rate for a Proca cloud of energy  $E$  would then be given by multiplying the ratio of the black points to the blue squares by  $(E/M)$ .

tion and the one including “Schwarzschild background corrections” in [8].

These results indicate that once the superradiant instability has extracted enough rotational energy from the black hole for the horizon frequency to decrease to the point where superradiance shuts off, the resulting Proca cloud can dissipate through GW radiation, in many cases faster than the time scales on which the higher  $m$  superradiant instabilities will operate.

#### IV. DISCUSSION AND CONCLUSION

We have used evolutions of the Proca equations on black holes spacetimes to study the superradiant instability for a range of parameters, finding that the growth rate for the field can be as high as  $3.6 \times 10^{-4} M^{-1}$  and  $2 \times 10^{-5} M^{-1}$  for modes with  $a = 0.99$  and  $m = 1$  and 2 azimuthal numbers, respectively. For larger values of the Proca mass, near where

the instability growth rate is maximized, the unstable modes are concentrated in the strong-field regime near the black hole horizon, and relativistic effects can be important. For the cases considered here (the fastest growing  $m = 1$  modes for spins  $0.7 \leq a \leq 0.99$  and  $m = 2$  modes for  $a = 0.99$ ) we have found that the frequency of the bound modes is well approximated by  $\omega_R \simeq \mu [1 - (\tilde{\mu}/m)^2/2 - (\tilde{\mu}/m)^3/3]$  where the last term is an additional relativistic correction to the hydrogenic approximation that we have rounded to a convenient fraction. This relativistic effect extends the range of mass parameters which are superradiantly unstable, and will also determine the black hole horizon frequency at which the instability will saturate [17] and be encoded in the frequency of any GWs sourced by such modes.

This can be used to look for, or place constraints on, the existence of ultralight vector fields using observations of spinning black holes, for example from observations of x-ray binaries, or from observing GW signals. As an example of how the results obtained here might translate into astrophysical terms, we note that a black hole formed from the merger of two equal mass, nonspinning black holes has a spin of approximately  $a \approx 0.7$ , which is consistent, within a 90% confidence interval, with the final black hole spins measured in the first two LIGO detections GW150914 and GW151226 [1, 2]. Using the above results for GW150914 (GW151226), the postmerger black hole with mass  $62 M_\odot$  ( $20.8 M_\odot$ ) would be superradiantly unstable with  $\tilde{\mu} = 0.18$  if there existed a massive vector boson with a physical mass of  $4 \times 10^{-13}$  eV ( $1 \times 10^{-12}$  eV). It would take roughly 180  $e$ -folds or 7 hours (2 hours) for a Proca cloud to grow from a single particle, to the level where it had liberated the  $E \approx 0.018M$  rotational energy from the black hole such that the horizon frequency matches  $\omega_R$ . The resulting Proca cloud would emit GWs at a frequency  $f_{\text{GW}} = \omega_R/\pi \approx 180$  Hz (550 Hz) with power  $P_{\text{GW}} \sim 10^{-10} \sim 10^{50}$  erg/s for time scales of  $E/P_{\text{GW}} \sim 11$  hours (4 hours). On a much longer timescale of years, the  $m = 2$  superradiant instability could also grow, and spin the black hole down even further.

This example is primarily for illustration, as the work of [8]—which explores the phenomenology of massive vector superradiance in detail—suggests that observations of x-ray binaries with rapidly spinning black holes have already excluded these particular vector boson masses, and more massive and/or rapidly spinning black hole mergers will be required to place further constraints.

### A. Comparison to other works

In this section we briefly compare the results obtained here to those in the literature. The methods used here are very similar to those in [32], which also used simulations to follow the evolution of Proca fields on a black hole spacetime, except without assuming an azimuthal symmetry as we do here. In [32] superradiant instability was observed in one simulation with  $a = 0.99$  and  $\tilde{\mu} = 0.4$  that exhibited strong beating of multiple modes with a quoted instability rate of  $M\omega_I \sim (5 \pm 1) \times 10^{-4}$ —or half that value, depending on the quantity measured. Here we obtain that  $M\omega_I \approx 2.4 \times 10^{-4}$  for the same parameters, consistent with the latter, and also find a value of  $M\omega_R \approx 0.36$  that matches the lower frequency component found there.

In this paper we have focused on studying the superradiant instability in the regime where the black hole spin and Proca mass parameter are not too small, since the long instability time scales would otherwise be too computationally expensive to follow with time-domain simulations. Nevertheless, we can also compare our results to those obtained in the nonrelativistic regime to see if there is a region of overlap, as we do in Fig. 12 for the fastest growing ( $m = 1$ ) mode. In [27], the authors study linear perturbations of massive vector fields around slowly rotating black holes and fit the instability rate they find to a function like the one used here [their Eq. (98)]; however, the overall coefficient they find for small spins is roughly an order of magnitude larger than the ones found here for large spins (which do increase with decreasing spin). Recently [8] have used a matching calculation to analytically compute superradiance rates in the nonrelativistic limit which is valid at small  $\tilde{\mu}$  but arbitrary spin. As shown in Fig. 12, their results agree quite well with those found here at  $a = 0.99$  and moderate values of  $\tilde{\mu}$ , and the difference is subpercent level at  $\tilde{\mu} = 0.2$ . At high values of  $\tilde{\mu}$ , the simulation results give faster instability rates, partly due to the relativistic corrections which reduce  $\omega_R$ . We also note that despite the good agreement of the fitting function Eq. (15) with the instability rate of [8] in the regime of moderate  $\tilde{\mu}$ , the latter is actually larger by a factor of  $\approx 2$  in the limit of  $\tilde{\mu} \rightarrow 0$ , indicating that these fitting functions do not fully capture the nonrelativistic limit. For lower values of black hole spin, it does appear that lower values  $\tilde{\mu}$  have to be used to get similar levels of agreement. For  $a = 0.7$  (also shown), we are not able to probe values  $\tilde{\mu}$  much below maximum instability, where the differences are more pronounced (though the fit extrapolated to small  $\tilde{\mu}$  is actually closer). In [19] the instability rate is com-

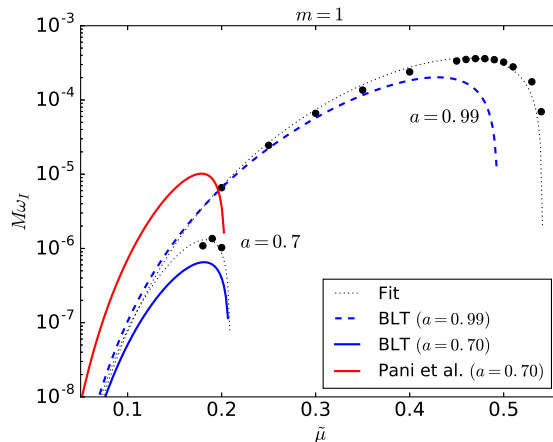


FIG. 12. A comparison of the instability growth rate for the dominant  $m = 1$  mode obtained here [black dots which are fit by the dotted curve, Eq. (15)] to the nonrelativistic approximation of [8] (blue curves) and the low-spin approximation of [27] (red curve) at two values of the black hole spin  $a = 0.7$  and  $0.99$ .

puted using an effective field theory approach, also assuming small  $\tilde{\mu}$ , and a similar scaling, but a larger coefficient is obtained. See [8] for a more detailed comparison of these different methods.

### B. Concluding remarks

We have explored the superradiant instability in the relativistic regime, determining the growth rate, frequency, gravitational radiation and other features of the dominant unstable modes. We have extended relativistic time-domain simulations to sufficiently large Compton wavelengths where they overlap with analytic results in the nonrelativistic limit, at least for rapidly spinning black holes. Though here we have focused on only the most unstable mode for the lowest two azimuthal numbers  $m$ , techniques similar to those used in [15] could be used to uncover a larger spectrum of modes from time simulations like the ones performed here. It would also be interesting to see if the relatively simple form for the instability growth rate and frequency found here could be derived analytically as a relativistic correction in perturbation theory.

In this study we have ignored the backreaction of the Proca field on the black hole spacetime, except to study the gravitational radiation in the weak field regime. This test field treatment will no longer be valid when the Proca grows large enough to extract

a non-negligible fraction of the black hole’s rotational energy. This regime is studied in [17] using these same methods as here, but evolving the full Einstein-Proca equations for select cases with a complex Proca field and an  $m = 1$  azimuthal symmetry. It is found that the superradiant instability smoothly saturates once the black hole has lost enough angular momentum for its horizon frequency to match the frequency of the Proca cloud that forms.<sup>2</sup> Another potential direction for future work is to study higher azimuthal number instabilities, as well as the possibility for interactions between different unstable modes making up a Proca cloud, in the nonlinear regime.

For the case of a single real-valued Proca field, we have found that the massive vector field hair that develops around a spinning black hole can efficiently radiate away through GW emission in the relativistic regime, on time scales that are only a few orders of magnitude longer than it took to develop. It would also be interesting to see how the details of the growth of the Proca cloud and decay through gravitational radiation play out in the fully nonlinear case.

#### ACKNOWLEDGMENTS

I thank Asimina Arvanitaki, Sam Dolan, Stephen Green, Luis Lehner, Jonah Miller, and Frans Pretorius for stimulating discussions. I am grateful to Masha Baryakhtar, Robert Lasenby, and Mae Teo for sharing their related work as it progressed. Simulations were run on the Perseus Cluster at Princeton University and the Sherlock Cluster at Stanford University. This research was supported in part by Perimeter Institute for Theoretical Physics. Research at Perimeter Institute is supported by the Government of Canada through the Department of Innovation, Science and Economic Development Canada and by the Province of Ontario through the Ministry of Research, Innovation and Science.

#### APPENDIX: CONVERGENCE RESULTS

To establish numerical convergence and estimate truncation error, we run select cases at three different resolutions, where the lowest has  $dx \approx 0.0256M$

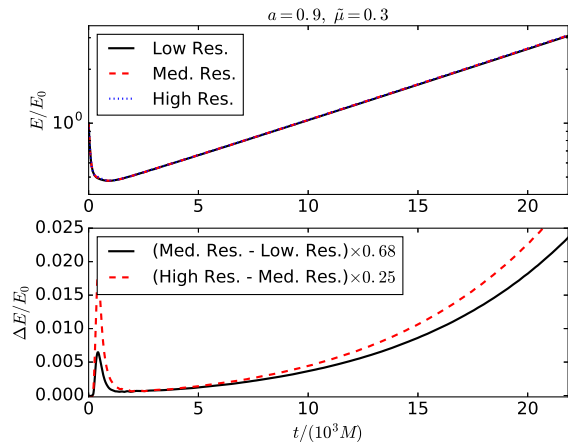


FIG. 13. Top: The energy in the Proca field as a function of time for a case with  $\tilde{\mu} = 0.3$ ,  $m = 1$  and a black hole with spin  $a = 0.9$ , at three different resolutions. Bottom: The difference in this quantity between resolutions, scaled assuming fourth-order convergence. The feature at early times is just truncation error from the numerical integration of the Proca energy, zeroed inside the black hole horizon, while a sizable fraction of the initial perturbation is falling into the black hole.

on the finest grid, and the medium and high resolutions have  $3/4$  and  $0.5\times$  smaller grid spacing, respectively. For all cases we use seven levels of mesh refinement, with 2:1 refinement ratio, centered on the black hole. In Fig. 13, we show the Proca field energy as a function of time for an example case at these three different resolutions. As expected, the error in this quantity is consistent with between third- and fourth-order convergence (with the quantities in the figure scaled assuming the latter).

As an estimate of the truncation error in computing the instability growth rate, we list the value of  $\omega_I$  found by fitting the energy to an exponential curve for several different cases, both as computed with the lowest resolution, and the Richardson extrapolated value from all three resolutions. The difference between the two values gives the approximate truncation error in this quantity at the lowest resolution. We can see that the error is greater for larger values of the mass parameter and spin. In the results presented in this paper, we use at least the medium resolution when  $\tilde{\mu}/m \geq 0.4$  (for  $m = 1$  and 2), and so we also list the values obtained at this resolution in Table I for higher mass parameters. With these choices for resolution, the truncation error in measuring  $\omega_I$  is  $\lesssim 5\%$  for the cases listed. The Proca field angular momentum shows very similar behavior to the energy, and in

<sup>2</sup>This is likely connected to the black hole with Proca hair solutions found in [21]; see also [9, 31] for studies of the analogous charged black hole case.

fact the ratio of these quantities at late times varies very little with resolution; e.g. for the cases mentioned in this section,  $E/J$  for the low and high resolutions differ by  $< 0.01\%$ .

TABLE I. A comparison of the instability growth rate for various cases at low (and medium for select cases) resolutions, to the Richardson extrapolated value using all three resolutions. This gives a measure of the truncation error.

$\tilde{\mu}$	$m$	$a$	$M\omega_I$ : Low res. (med res.)	Rich. ext.
0.3	1	0.90	$4.59 \times 10^{-5}$	$4.60 \times 10^{-5}$
0.3	1	0.99	$6.58 \times 10^{-5}$	$6.62 \times 10^{-5}$
0.4	1	0.99	$2.36 \times 10^{-4}$	$2.31 \times 10^{-4}$
0.5	1	0.99	$3.0 \times 10^{-4}$ ( $3.2 \times 10^{-4}$ )	$3.3 \times 10^{-4}$
0.95	2	0.99	$1.6 \times 10^{-5}$ ( $1.9 \times 10^{-5}$ )	$2.0 \times 10^{-5}$

In addition to truncation error, there will also be systematic error due to the presence of other modes in addition to the most unstable one, confounding the measurement. In general, this will bias the measured growth rate towards lower values, and the frequency towards higher values. This is more difficult to estimate since it depends on how much the initial perturbation excites the other modes, and what their growth is relative to the most unstable mode. The effects of this will decrease the longer each case is involved, but will likely be the dominant source of error for the cases with slower growth  $\omega_I \lesssim 10^{-5}M^{-1}$ , since we do not consider evolutions longer than  $\sim 10^5M$  for computational reasons. As a rough indication of this, we note that for the smallest  $\tilde{\mu}$  (leftmost) points in Figs. 5 and 6, if we instead use half the simulation time to measure the instability rate, we obtain values that are 0.01% and 4% lower, respectively.

- 
- [1] Abbott, B. P. *et al.* (Virgo, LIGO Scientific), *Phys. Rev. Lett.* **116**, 241103 (2016), arXiv:1606.04855 [gr-qc].
- [2] Abbott, B. P. *et al.* (Virgo, LIGO Scientific), *Phys. Rev. Lett.* **116**, 061102 (2016), arXiv:1602.03837 [gr-qc].
- [3] Abbott, B. P. *et al.* (Virgo, LIGO Scientific), *Astrophys. J.* **833**, L1 (2016), arXiv:1602.03842 [astro-ph.HE].
- [4] Arvanitaki, A., Baryakhtar, M., Dimopoulos, S., Dubovsky, S., and Lasenby, R., *Phys. Rev.* **D95**, 043001 (2017), arXiv:1604.03958 [hep-ph].
- [5] Arvanitaki, A., Baryakhtar, M., and Huang, X., *Phys. Rev.* **D91**, 084011 (2015), arXiv:1411.2263 [hep-ph].
- [6] Arvanitaki, A., Dimopoulos, S., Dubovsky, S., Kaloper, N., and March-Russell, J., *Phys. Rev.* **D81**, 123530 (2010), arXiv:0905.4720 [hep-th].
- [7] Arvanitaki, A. and Dubovsky, S., *Phys. Rev.* **D83**, 044026 (2011), arXiv:1004.3558 [hep-th].
- [8] Baryakhtar, M., Lasenby, R., and Teo, M., (2017), arXiv:1704.05081 [hep-ph].
- [9] Bosch, P., Green, S. R., and Lehner, L., *Phys. Rev. Lett.* **116**, 141102 (2016), arXiv:1601.01384 [gr-qc].
- [10] Brito, R., Cardoso, V., and Pani, P., *Class. Quant. Grav.* **32**, 134001 (2015), arXiv:1411.0686 [gr-qc].
- [11] Choquet, M. W., Hirschmann, E. W., Liebling, S. L., and Pretorius, F., *Phys. Rev.* **D68**, 044007 (2003), arXiv:gr-qc/0305003 [gr-qc].
- [12] Damour, T., Deruelle, N., and Ruffini, R., *Lettere Al Nuovo Cimento Series 2* **15**, 257 (1976).
- [13] Detweiler, S. L., *Phys. Rev.* **D22**, 2323 (1980).
- [14] Dolan, S. R., *Phys. Rev.* **D76**, 084001 (2007), arXiv:0705.2880 [gr-qc].
- [15] Dolan, S. R., *Phys. Rev.* **D87**, 124026 (2013), arXiv:1212.1477 [gr-qc].
- [16] East, W. E. and Pretorius, F., *Phys. Rev.* **D87**, 101502 (2013), arXiv:1303.1540 [gr-qc].
- [17] East, W. E. and Pretorius, F., (2017), arXiv:1704.04791 [gr-qc].
- [18] East, W. E., Ramazanoglu, F. M., and Pretorius, F., *Phys. Rev.* **D89**, 061503 (2014), arXiv:1312.4529 [gr-qc].
- [19] Endlich, S. and Penco, R., (2016), arXiv:1609.06723 [hep-th].
- [20] Gal'tsov, D. V., Pomerantseva, G. V., and Chizhov, G. A., *Sov. Phys. J.* **27**, 697 (1984), [Izv. Vuz. Fiz.27,81(1984)].
- [21] Herdeiro, C., Radu, E., and Runarsson, H., *Class. Quant. Grav.* **33**, 154001 (2016), arXiv:1603.02687 [gr-qc].
- [22] Holdom, B., *Phys. Lett.* **B166**, 196 (1986).
- [23] Kerr, R. P. and Schild, A., in *IV Centenario Della Nascita di Galileo Galilei* (1965) p. 222.
- [24] Konoplya, R. A., *Phys. Rev.* **D73**, 024009 (2006), arXiv:gr-qc/0509026 [gr-qc].
- [25] Konoplya, R. A. and Molina, C., *Phys. Rev.* **D75**, 084004 (2007), arXiv:gr-qc/0602047 [gr-qc].
- [26] Pani, P., Cardoso, V., Gualtieri, L., Berti, E., and Ishibashi, A., *Phys. Rev. Lett.* **109**, 131102 (2012), arXiv:1209.0465 [gr-qc].
- [27] Pani, P., Cardoso, V., Gualtieri, L., Berti, E., and Ishibashi, A., *Phys. Rev.* **D86**, 104017 (2012), arXiv:1209.0773 [gr-qc].
- [28] Press, W. H. and Teukolsky, S. A., *Nature (London)* **238**, 211 (1972).
- [29] Pretorius, F., *Class. Quant. Grav.* **22**, 425 (2005), arXiv:gr-qc/0407110 [gr-qc].
- [30] Rosa, J. G. and Dolan, S. R., *Phys. Rev.* **D85**, 044043 (2012), arXiv:1110.4494 [hep-th].

- [31] Sanchis-Gual, N., Degollado, J. C., Montero, P. J., Font, J. A., and Herdeiro, C., *Phys. Rev. Lett.* **116**, 141101 (2016), arXiv:1512.05358 [gr-qc].
- [32] Witek, H., Cardoso, V., Ishibashi, A., and Sperhake, U., *Phys. Rev.* **D87**, 043513 (2013), arXiv:1212.0551 [gr-qc].
- [33] Yoshino, H. and Kodama, H., *PTEP* **2014**, 043E02 (2014), arXiv:1312.2326 [gr-qc].
- [34] Zilhão, M., Witek, H., and Cardoso, V., *Class. Quant. Grav.* **32**, 234003 (2015), arXiv:1505.00797 [gr-qc].
- [35] Zouros, T. and Eardley, D., *Annals Phys.* **118**, 139 (1979).